Hindawi
International Journal of Energy Research
Volume 2024, Article ID 2936714, 15 pages
https://doi.org/10.1155/2024/2936714

Research Article

Effects of Varying Annealing Ambient towards Performance of Ternary $Ga_xCe_yO_z$ Passivation Layers for Metal-Oxide-Semiconductor Capacitor

Kammutty Musliyarakath Abdul Shekkeer,[1] **Kuan Yew Cheong**,[2] **and Hock Jin Quah**[1]

[1]*Institute of Nano Optoelectronics Research and Technology (INOR), Universiti Sains Malaysia, George Town 11800, Penang, Malaysia*
[2]*School of Materials and Mineral Resources Engineering, Universiti Sains Malaysia, 14300, Nibong Tebal, George Town, Penang, Malaysia*

Correspondence should be addressed to Hock Jin Quah; hock_jin@usm.my

Received 14 September 2023; Revised 25 December 2023; Accepted 5 February 2024; Published 16 February 2024

Academic Editor: Tholkappiyan Ramachandran

Copyright © 2024 Kammutty Musliyarakath Abdul Shekkeer et al. This is an open access article distributed under the Creative Commons Attribution License, which permits unrestricted use, distribution, and reproduction in any medium, provided the original work is properly cited.

In this work, different annealing ambient (nitrogen-oxygen-nitrogen (N_2-O_2-N_2), forming gas-oxygen-forming gas (FG-O_2-FG), and argon-oxygen-argon (Ar-O_2-Ar)) were explored to investigate the feasibility of employing the annealed ternary $Ga_xCe_yO_z$ passivation layer (PL) for development of Si-based metal-oxide-semiconductor (MOS) capacitors. The impact of nitrogen and/or hydrogen in hindering the growth of silicon dioxide (SiO_2) interfacial layer (IL) was quantitatively evaluated. The combination of effects brought by nitrogen attached to oxygen vacancies, nitrogen-silicon bonding, and nitrogen accumulation at the $Ga_xCe_yO_z$/Si interface effectively minimized the formation of SiO_2 IL. Consequently, among all the samples, the $Ga_xCe_yO_z$ PL annealed in N_2-O_2-N_2 ambient exhibited superior MOS characteristics in terms of low effective oxide charge, slow trap density, interface trap density, and interface state density, which have translated into good leakage current density-electric field characteristics.

1. Introduction

The persistent downscaling of complementary metal-oxide-semiconductor (CMOS) devices, which are the foundation of silicon- (Si-) integrated circuits (IC), serves to enhance device packing density and minimizes power consumption of advanced electronic devices [1]. Consequently, the growing demand of high-performance electronic devices has pushed the scaling of device dimension to its limit, whereby the employment of ultrathin silicon dioxide (SiO_2) gate oxide as passivation layer (PL) in Si-based MOS devices would increase the probability of electrons tunnelling through the trapezoidal energy barrier [2]. Inevitably, the occurrence of this direct tunnelling mechanism would promote the undesirable leakage current during the operation of Si-based MOS devices contributing towards the generation of additional heat as well as reliability issues [3]. Therefore, it is necessary to substitute the conventional SiO_2 possessing a low dielectric constant ($k = 3.9$) with a high-k material as PL for Si-based MOS devices [4]. The employment of high-k material would allow the utilization of a physically thicker PL as well as higher gate capacitance for Si-based MOS devices, which would ultimately lead to the accumulation of more charge carriers at the Si channel [5]. Therefore, the utilization of high-k material as a PL in fabricated Si-based MOS devices could potentially result in the ability to simultaneously endure a higher electric breakdown field and a lower leakage current density [5, 6]. To this day, a vast range of high-k substances, such as Al_2O_3 [7], CeO_2 [8], Yb_2O_3 [9], ZrO_2 [10], HfO_2 [11], Nd_2O_3 [12], La_2O_3 [13], MgO [14], and Tm_2O_3 [15], have been studied as possible alternatives to SiO_2 as the PL for Si-based MOS devices.

Among these investigated high-k materials, CeO_2 has leaped into the forefront to replace conventional SiO_2 as

the PL for Si-based MOS devices due to the intriguing features of CeO_2, such as high-k values ranging from 10 to 16 [8, 16], large bandgap ranging from 3.0 to 3.6 eV [8, 17], low interface state density ($<10^{11}\,cm^{-2}\,eV^{-1}$) [18], low stress-induced defect formation [19], and low lattice mismatch with the Si substrate [20]. The utilization of a physically thicker, high-k CeO_2 PL would effectively reduce the occurrence of leakage current governed by direct tunnelling mechanism that would result in an improvement in the electric breakdown field of the Si-based MOS device with the usage of CeO_2 PL [21]. It was proven in previous research that Si-based MOS capacitor with CeO_2 PL subjected to a combination of post-nitrous oxide (N_2O) plasma treatment and rapid thermal annealing in nitrogen ambient was able to withstand a high electric breakdown field of 24.67 MV/cm [22]. The versatility of CeO_2 to be employed in the applications, such as energy storage, catalysts, and electrochemical devices, was due to its reversible transition from oxidation state of Ce^{4+} to reduction state of Ce^{3+}, but the feasibility of utilizing this characteristic for passivation layer was deemed to be quite challenging [23, 24]. Earlier studies indicated that although CeO_2 has shown the potential as a PL for Si-based MOS devices, the issue of partial reducibility of Ce^{4+} to Ce^{3+} states remained present as a challenge due to the polaron hopping mechanism that occurred between localized states within the forbidden gap, resulting in an increase in leakage current through the CeO_2 PL [25, 26]. The occurrence of this reducibility effect hampering the passivating property of CeO_2 PL was due to the formation of oxygen vacancies [16, 27] that would augment the diffusion of oxygen by modifying the valance state of CeO_2, as observed in prior studies [26, 28]. Consequently, there was an increase in the growth of the low-k SiO_2 IL due to the availability of a larger number of oxygen ions to diffuse to the Si surface [27]. Besides, the formation of oxygen vacancies in the CeO_2 PL would also act as a shallow trap that would promote an increase in leakage current density [29, 30].

In order to circumvent the above-mentioned issue, an initial approach of improving the passivating properties of CeO_2 was through the doping of tetravalent cations, such as Zr^{4+} [31], Sn^{4+} [32], Si^{4+} [33], Ti^{4+} [34], and Hf^{4+} [35] into the CeO_2 crystal lattice. Unfortunately, prior studies have revealed that the doping of tetravalent cations into the crystal lattice of CeO_2 has reduced the energy required for defect formation, which in turn promoted the creation of additional oxygen vacancies [36, 37]. Thus, the creation of additional deep states within the bandgap of the investigated tetravalent doped CeO_2 would contribute to bandgap narrowing as well as promoting leakage current [27, 36, 38]. Consequently, the use of trivalent cations (M^{3+}), such as Mn^{3+}, Gd^{3+}, Sc^{3+}, La^{3+}, Ho^{3+}, Er^{3+}, and Y^{3+} ions as a dopant for CeO_2, has become the focus of research as a lower energy is required to dope the M^{3+} ions into CeO_2 lattice compared to generating oxygen vacancies through CeO_2 phase reduction [39, 40]. Although doping of CeO_2 by M^{3+} leads to the emergence of additional oxygen vacancies to maintain electroneutrality, the ability to forge a strong coulombic interaction between the trivalent ions and oxygen vacancies would give rise to the formation of vacancy dopant defect clusters (M^{3+}-V_o) [41, 42]. The generation of M^{3+}-V_o defect pair in CeO_2-doped trivalent ions would increase the energy barrier for oxygen migration [43], thereby limiting the accumulation of oxygen ions at the interface. The generation of M^{3+}-V_o defect pair has been found to exhibit a beneficial effect on Sc^{3+}-, Ho^{3+}-, and Er^{3+}-doped CeO_2, whereby these M^{3+} ions would serve as scavengers of oxygen vacancies, inhibiting the diffusion of oxygen ions towards the interface [40, 44]. Moreover, the strength of the interaction between M^{3+}-V_o defect pair was found to be significantly influenced by the ionic radius difference among the trivalent ions and Ce^{4+} ions, indicating that the doping of trivalent ions having smaller ionic radii could lead to the strengthening of the interaction between these ions and oxygen vacancies, ultimately leading to the inhibition of oxygen diffusion [41].

This study proposes to use trivalent gallium (Ga^{3+}) ions doped into the CeO_2 crystal lattice to form a ternary $Ga_xCe_yO_z$, whereby a larger difference in ionic radius between the Ga^{3+} ion (0.62 Å) [45] and the Ce^{4+} ion (0.97 Å) [46] would translate to a stronger coulombic interaction between Ga^{3+} and oxygen vacancies, thereby restricting oxygen ions from diffusing to the interface [47]. Additionally, the passivating properties of the $Ga_xCe_yO_z$ PL could be improved due to the excellent properties of Ga_2O_3, which includes the possession of a larger bandgap of 4.9 eV [48] as well as high-k values (10.2-14.2) [49, 50]. Optimizing the postdeposition annealing parameters is crucial to further improve passivating characteristics of the $Ga_xCe_yO_z$ PL, as previous research has revealed that the $Ga_xCe_yO_z$ PL annealed at 700°C in a nitrogen-oxygen-nitrogen (N_2-O_2-N_2) ambient has shown the best MOS characteristics in terms of the minimum leakage current density, maximum k value, and the largest bandgap [51]. Moreover, the process of annealing at a temperature of 700°C in N_2-O_2-N_2 ambient was found to be highly effective in regulating the growth of the SiO_2 IL [51]. This was due to the existence of nitrogen ions which actively participated in attaching to the oxygen vacancies, thereby hampering oxygen ions from diffusing to the interface [51]. It is worth highlighting that oxygen gas was introduced during dwelling stages regardless of the employment of different gases during the heating and cooling stages with the purpose of repairing the oxygen-related defects and broken bonds [52]. It was proven in other research works that a reduction in interface trap density [53, 54] and fixed oxide charge [55, 56] as well as a low leakage current [57, 58] and negligible hysteresis [59, 60] was reported when the high-k materials acting as PL were subjected to postdeposition annealing in oxygen ambient. Nevertheless, postdeposition annealing in oxygen ambient would result in an exaggeration in the formation of SiO_2 IL between the high-k PL and Si substrate [61]. Hence, previous investigation on high-k materials as the PL has diverted towards the usage of nitrogen ambient during postdeposition annealing process for the nitrogen ions to diffuse to the interface between the PL and Si substrate, to accumulate, and to form a barrier layer in order to impede the formation of SiO_2 interfacial layer [62]. Moreover, the utilization of ambient comprising of nitrogen and hydrogen gases during postdeposition annealing would facilitate the reduction of defect states and

the improvement of interface quality by passivating the Si dangling bonds with either the hydrogen or the nitrogen, as well as by having the nitrogen to attach to oxygen vacancies, which would eventually improve leakage current density and breakdown field of the Si-based MOS devices [63, 64]. Besides nitrogen and hydrogen gases, the beneficial effects of utilizing argon ambient during postdeposition annealing were also being highlighted for other high-k PL, wherein an improvement in leakage current density, interface trap density, and effective oxide charge, as well as the mitigation in the formation of SiO_2 interfacial layer, was reported when argon ambient was being used [65, 66]. Dissimilar from previous work, this work intends to utilize different combinations of gases during postdeposition annealing process, whereby different gases will be used during the heating and cooling stages while oxygen gas will be kept the same during the dwelling stage of the postdeposition annealing process. Hence, a combination of forming gas-oxygen-forming gas (FG-O_2-FG), nitrogen-oxygen-nitrogen (N_2-O_2-N_2) [51], and argon-oxygen-argon (Ar-O_2-Ar) at 700°C was used to provide a comparative study on the structural, morphological, optical, and metal-oxide-semiconductor (MOS) characteristics of $Ga_xCe_yO_z$ PL deposited on Si substrate, which has not been reported in previous works.

2. Experimental

The 4-inch n-type Si substrate (100) orientation was sliced into 1 cm^2 dimension and subjected to standard Radio Corporation of America (RCA) cleaning process. Following that, the RCA cleaned samples were immersed in a diluted hydrofluoric (HF) acid solution to etch the native oxide of SiO_2 from the surface of Si substrate. It was highlighted in previous research works on the importance of chemical purity in the formation of a high-quality passivation layer, wherein all chemicals being used in this work are having a purity level of 99.99% [67, 68]. Initially, 0.191 g of gallium(III) nitrate hydrate (Sigma-Aldrich, 99.99%) was dissolved in 5 ml of methanol (J.T. Baker, analytical grade) and stirred for 15 min at 30°C on a hot plate to form a 0.25 M gallium-containing precursor. Subsequently, 1.0936 g of cerium(III) acetylacetonate hydrate (Sigma-Aldrich, 99.99%) was dissolved in 3 ml of methanol (J.T. Baker, analytical grade) and 6 ml of acetic acid (J.T. Baker, CMOS grade) and stirred for 15 min at 60°C to prepare a 0.25 M cerium-containing precursor. Finally, the cerium- and gallium-containing precursors were stirred continuously for 30 min at 60°C to obtain a ratio of 1 : 1. Then, the resulting $Ga_xCe_yO_z$ precursor was cooled down to room temperature. Subsequently, the $Ga_xCe_yO_z$ precursor was spin-coated on an RCA-clean n-type Si substrate with an rpm of 3000 for 30 s. These as-deposited samples were subjected to postdeposition annealing in different ambient of FG-O_2-FG, N_2-O_2-N_2, and Ar-O_2-Ar for 30 min at 700°C in a quartz tube furnace. During the heating and cooling stages, FG or N_2 or Ar (100 ml/min) was flown into the furnace while O_2 gas with a similar flow rate was employed during the dwelling stage. After completing the postdeposition annealing process, the Al/$Ga_xCe_yO_z$/Si/Al MOS capacitors were realised by evaporating aluminium (Al) contact on the surface of the $Ga_xCe_yO_z$ PL using a shadow mask (diameter = 0.2 mm) and a layer of Al was deposited as the back contact on Si substrate.

Crystalline phase and orientation of the investigated $Ga_xCe_yO_z$ PL subjected to different postdeposition annealing ambient were characterized using grazing incident X-ray diffraction (GIXRD; Bruker D8 Discover) analysis. The surface morphologies and cross sectional images, as well as elemental composition of the investigated $Ga_xCe_yO_z$ PL, were carried out using field-emission scanning electron microscopy (FESEM; FEI Nova NanoSEM 450) equipped with energy dispersive X-ray analysis (EDX; JSM-6460 LV). The estimation of thickness for the $Ga_xCe_yO_z$ PL and SiO_2 IL was determined based on the acquired X-ray reflectivity (XRR) results measured using Bruker D8 Discover. 3-dimensional topographies as well as root-mean-square (RMS) roughness of the investigated $Ga_xCe_yO_z$ PL were characterized using atomic force microscopy (AFM; Dimension Edge, Bruker). The bandgap of investigated $Ga_xCe_yO_z$ PL was extracted from diffused reflectance spectra acquired using ultraviolet–visible (UVVIS) spectrophotometer (Cary 5000). The capacitance-voltage (C-V) and current-voltage (I-V) characteristics of the investigated samples were measured using Keithley 4200-SCS parameter analyzer.

3. Results and Discussions

3.1. Structural, Chemical, and Optical Characteristics of $Ga_xCe_yO_z$ PL Annealed in FG-O_2-FG, N_2-O_2-N_2, and Ar-O_2-Ar Ambient. The GIXRD pattern as represented in Figure 1 indicates that the $Ga_xCe_yO_z$ PL annealed in FG-O_2-FG, N_2-O_2-N_2, and Ar-O_2-Ar ambient at 700°C have emerged as polycrystalline, with the detection of $Ga_xCe_yO_z$ phase oriented in (111), (200), (220), and (311) planes for all of the $Ga_xCe_yO_z$ PL, which were indexed with the International Centre for Diffraction Data (ICDD) file no. 00-034-0394 for cubic fluorite CeO_2 phase. Additionally, it was also perceived that no additional phases with regard to either cubic Ga_2O_3 (ICDD file no. 00-020-0426) or monoclinic Ga_2O_3 (ICDD file no. 00-041-1103) phases were detected from the attained GIXRD results indicating that no phase separation has taken place. Furthermore, it was observed that the GIXRD peaks associated with the $Ga_xCe_yO_z$ phase exhibited a displacement towards a higher diffraction angle in contrast to the CeO_2 phase documented in the ICDD file no. 00-034-0394. This could be an indication that Ga^{3+} ions having a smaller ionic radius of 0.62 Å than Ce^{4+} ions (0.97 Å) have successfully doped into the CeO_2 crystal framework to form ternary $Ga_xCe_yO_z$ phase.

The lattice parameter a of the investigated $Ga_xCe_yO_z$ PL was determined based on the equation given below [69]:

$$n\lambda = 2d_{hkl} \sin\theta,$$
$$\frac{1}{d_{hkl}^2} = \frac{h^2 + k^2 + l^2}{a^2}, \quad (1)$$

where d_{hkl}, θ, and hkl are the interplanar spacing, diffraction angle, and Miller's index, respectively. Table 1 presents the

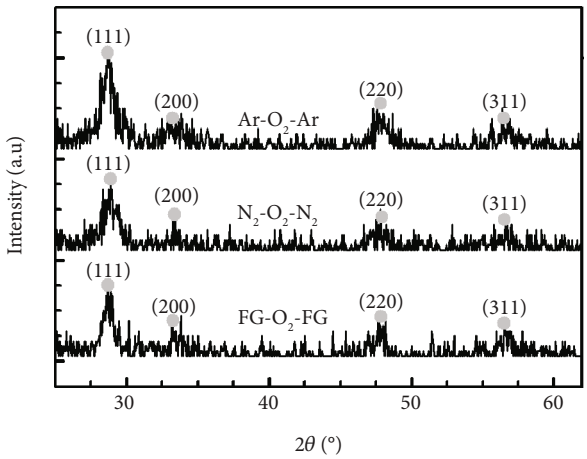

Figure 1: GIXRD patterns of $Ga_xCe_yO_z$ PL annealed in different ambient of N_2-O_2-N_2 [51], FG-O_2-FG, and Ar-O_2-Ar.

calculated lattice parameter *a* for the investigated $Ga_xCe_yO_z$ PL subjected to annealing at 700°C in different ambient. It has been noted that all $Ga_xCe_yO_z$ PL have undergone lattice contraction in comparison to standard CeO_2, which has a lattice parameter of 0.5411 nm [70]. This observation supports the successful doping of Ga^{3+} ions, which have a smaller ionic radius than Ce^{4+} ions, into the CeO_2 crystal lattice, resulting in the formation of a ternary $Ga_xCe_yO_z$ phase. Of these investigated $Ga_xCe_yO_z$ PL, it was noticed that $Ga_xCe_yO_z$ PL annealed in N_2-O_2-N_2 ambient has attained the smallest lattice parameter *a* (Table 1). The observation at hand may potentially be attributed to the generation of an elevated concentration of oxygen vacancies within the $Ga_xCe_yO_z$ PL during the annealing process in N_2-O_2-N_2 ambient. This, in turn, could result in the attachment of nitrogen ions to the generated oxygen vacancies, hence leading to the release of adjacent oxygen ions from the $Ga_xCe_yO_z$ lattice as a means of achieving charge neutrality [51]. It was noticed that a smaller reduction in the lattice parameter *a* was attained for $Ga_xCe_yO_z$ PL subjected to annealing in FG-O_2-FG ambient compared to N_2-O_2-N_2 ambient. The aforementioned observation implied that the coexistence of hydrogen and nitrogen ions during annealing in an FG-O_2-FG ambient would result in the hydrogen ions, which possess a smaller ionic radius (0.0290 nm) [71] in comparison to the nitrogen ions (0.1460 nm) [72], diffusing at a faster rate to attach with the oxygen vacancies in the $Ga_xCe_yO_z$ lattice. Subsequently, the nitrogen ions from the FG-O_2-FG ambient that were diffusing at a slower rate would be attached to the unoccupied oxygen vacancies in the $Ga_xCe_yO_z$ lattice in which an excess of negative charges would be generated in the $Ga_xCe_yO_z$ PL annealed in FG-O_2-FG ambient. Nevertheless, due to the earlier attachment of hydrogen ions with oxygen vacancies that have contributed to the generation of an excess positive charges in the $Ga_xCe_yO_z$ lattice, charge compensation has taken place and the release of adjacent oxygen ions to achieve charge neutrality in the $Ga_xCe_yO_z$ PL annealed in FG-O_2-FG ambient was not required. Upon analysis, it was observed that the peaks corresponding to the $Ga_xCe_yO_z$ phase in the PL annealed in the FG-O_2-FG ambient have shifted towards smaller diffraction angles in comparison to the N_2-O_2-N_2 ambient. This finding serves as substantiating proof that the generation of oxygen vacancies in the $Ga_xCe_yO_z$ PL was reduced in the FG-O_2-FG ambient. Since postdeposition annealing carried out in Ar-O_2-Ar ambient did not involve the incorporation of nitrogen and/or hydrogen ions into the $Ga_xCe_yO_z$ lattice, the attachment of the ions to oxygen vacancies would not happen, and therefore, supposedly the amount of oxygen vacancies present in the $Ga_xCe_yO_z$ PL could be the most significant when compared with the other two ambient, and an abrupt decrease in the lattice parameter *a* should be expected. Nevertheless, it was noticed that the attained lattice parameter *a* for this sample (0.5387 nm) was close to the lattice parameter *a* of the standard CeO_2 sample (0.5411 nm) and to be specific was smaller than CeO_2. This disparity indicated that the acquisition of a similar lattice parameter *a* was linked to the doping of Ga^{3+} into the CeO_2 crystal lattice, as opposed to the result of either nitrogen or hydrogen ions attached with the oxygen vacancies.

Table 1: Lattice parameter *a*, crystallite size *D*, and microstrain ε for $Ga_xCe_yO_z$ PL annealed in different ambient of N_2-O_2-N_2 [51], FG-O_2-FG, and Ar-O_2-Ar as well as lattice parameter *a* for standard CeO_2.

Annealing ambient	Lattice parameter *a* (nm)	Crystallite size *D* (nm)	Microstrain ε
N_2-O_2-N_2	0.5350	15.92	0.0072
FG-O_2-FG	0.5380	13.87	0.0057
Ar-O_2-Ar	0.5387	19.99	0.0109
Standard CeO_2	0.5411	—	—

Further scrutiny was conducted through the utilization of EDX analysis on the scrutinized $Ga_xCe_yO_z$ PL, and the resulting findings are subsequently depicted in Table 2. It was perceived that the sample annealed in FG-O_2-FG ambient attained a higher atomic percentage (at%) of nitrogen when compared to N_2-O_2-N_2 ambient although the employment of forming gas ambient was contained of a lower proportion of nitrogen (90%) in contrast to pure nitrogen ambient. The aforementioned observation has served to bolster the prior postulation that the utilization of FG-O_2-FG ambient would incite the initial attachment of hydrogen ions to the oxygen vacancies, owing to the superior diffusion rate of hydrogen ions as compared to nitrogen ions. Since the ionic radius of hydrogen ions was smaller than that of nitrogen ions, the attachment of hydrogen ions to the oxygen vacancies would provide sufficient space in the lattice for the passage of the nitrogen ions to the interface between the $Ga_xCe_yO_z$ PL and Si substrate when compared with the attachment of nitrogen ions to the oxygen vacancies. Consequently, the outcome of the postdeposition annealing process in FG-O_2-FG ambient was the buildup of a higher concentrations of nitrogen ions at the interface to act as a more potent oxygen diffusion barrier layer, which is highly effective in hindering the formation of SiO_2 IL. The lower value of at% of nitrogen in the $Ga_xCe_yO_z$ PL annealed in N_2-O_2-N_2 ambient could be due to the higher likelihood of

Table 2: Elemental composition for the $Ga_xCe_yO_z$ PL annealed in different ambient of N_2-O_2-N_2 [51], FG-O_2-FG, and Ar-O_2-Ar.

Annealing ambient	O (at. %)	Ce (at. %)	Ga (at. %)	N (at. %)
N_2-O_2-N_2	69.45	16.89	9.80	3.85
FG-O_2-FG	69.84	16.09	9.43	4.64
Ar-O_2-Ar	64.92	24.34	10.73	—

nitrogen ions attaching to the oxygen vacancies, wherein narrower spacing within the $Ga_xCe_yO_z$ lattice would impede the nitrogen ions from diffusing towards the interface. This indicates that the initially inward diffusing nitrogen ions that were unable to form attachment with oxygen vacancies or diffuse to the interface between $Ga_xCe_yO_z$ PL and Si substrate would subsequently diffuse out of the PL aiding in the acquisition of a lower at% of nitrogen during annealing in N_2-O_2-N_2 ambient. It was noticed that the acquisition of a higher at% of oxygen for $Ga_xCe_yO_z$ PL annealed in FG-O_2-FG ambient when compared with N_2-O_2-N_2 ambient has further reinforced that the simultaneous attachment of hydrogen and nitrogen ions with oxygen vacancies has minimized the release of oxygen ions from $Ga_xCe_yO_z$ lattice. Nevertheless, it was perceived that Ar-O_2-Ar ambient has led to the attainment of the minimum at% of oxygen in $Ga_xCe_yO_z$ PL, but it did not necessarily translate into large amount of oxygen vacancies as evidenced by the close lattice parameter a between CeO_2 and $Ga_xCe_yO_z$.

The FESEM images of the examined $Ga_xCe_yO_z$ PL shown in Figure 2 could be utilized to analyze the effectiveness of nitrogen and/or hydrogen ions in hindering the formation of SiO_2 IL. The total oxide thickness of the investigated PL was calculated from 10 distinct points, as illustrated in Table 3. It was deduced that the existence of nitrogen and/or hydrogen ions was effective in minimizing the formation of SiO_2 IL as the average total oxide thickness obtained by both $Ga_xCe_yO_z$ PL subjected to postdeposition annealing in N_2-O_2-N_2 (30.41 nm) and FG-O_2-FG ambient (40.16 nm) was lower than that of Ar-O_2-Ar (53.75 nm). In addition, it was also divulged that FG-O_2-FG ambient was not as effective as N_2-O_2-N_2 ambient in retarding the diffusion of oxygen ions to react with Si surface as a larger average total oxide thickness was attained by the $Ga_xCe_yO_z$ PL annealed in FG-O_2-FG ambient. The proposition being put forward posited that the accumulation of hydrogen ions at the interface may be comparatively inadequate in impeding the diffusion of oxygen ions towards the interface, in contrast to the accumulation of nitrogen ions at the same interface. It was hypothesised that the accumulation of hydrogen ions with a smaller ionic radius at the interface and a weaker bond strength between the hydrogen ions and Si [68] would enable the oxygen ions to either bypass or disrupt these bonds, leading to the reaction with the underlying Si surface during annealing in FG-O_2-FG ambient. This reaction would contribute to the development of a thicker SiO_2 IL in comparison to N_2-O_2-N_2 ambient.

To ascertain the thickness of the $Ga_xCe_yO_z$ PL and SiO_2 IL subjected to annealing in varying postdeposition annealing ambient, the resulting XRR data was subjected to fitting

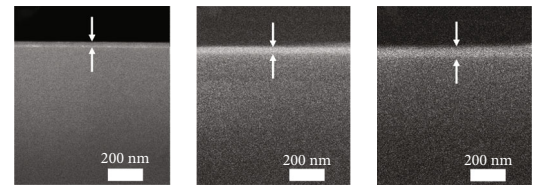

Figure 2: Cross-sectional FESEM images of $Ga_xCe_yO_z$ PL annealed in (a) N_2-O_2-N_2, (b) FG-O_2-FG, and (c) Ar-O_2-Ar ambient.

procedures using the Bruker DIFFRAC Leptos software (version 7.10.0.12). The XRR experimental and fitted results for the investigated $Ga_xCe_yO_z$ PL are illustrated in Figure 3. Outcome from the analysis of the XRR findings, it was further reinforced that the accumulation of nitrogen ions at the interface as well as the bonding between the nitrogen ions and Si were less susceptible for the oxygen ions to bypass the accumulated nitrogen ions at the interface as well as breaking the bonding between nitrogen ions and Si. Thus, the lowest thickness of SiO_2 IL (0.96 nm) was attained for the $Ga_xCe_yO_z$ PL annealed in N_2-O_2-N_2 ambient. Nonetheless, thicker SiO_2 IL was formed for $Ga_xCe_yO_z$ PL annealed in FG-O_2-FG (2.32 nm) and Ar-O_2-Ar (6.94 nm) denoting that the oxygen ions diffusing towards the interface region were less retarded when compared with N_2-O_2-N_2 ambient. The activation energy (E_a) related to the growth of SiO_2 IL or the densification of $Ga_xCe_yO_z$ PL postdeposition annealed in different ambient could be calculated using the subsequent equation [73]:

$$t = t_o \exp(-), \tag{2}$$

where t is the thickness of SiO_2 IL or $Ga_xCe_yO_z$ PL after postdeposition annealing in different ambient, t_o is the thickness of SiO_2 IL (0.20 nm) or $Ga_xCe_yO_z$ PL (160.64 nm) for the as-deposited sample [51], k is Boltzmann's constant, and T is the postdeposition annealing temperature in Kelvin. The PL that underwent annealing in Ar-O_2-Ar and FG-O_2-FG ambient had larger E_a values of 2.603×10^{-1} and 2.533×10^{-1} eV, respectively, indicating an exaggerated formation of SiO_2 IL when compared to N_2-O_2-N_2 ambient (1.287×10^{-1} eV). Besides, it was also observed that all of the investigated $Ga_xCe_yO_z$ PL were undergoing densification process due to the acquisition of E_a of 1.462×10^{-1}, 1.356×10^{-1}, and 0.932×10^{-1} eV for N_2-O_2-N_2, FG-O_2-FG, and Ar-O_2-Ar ambient, respectively. It was postulated that the acquisition of the smallest E_a by $Ga_xCe_yO_z$ PL annealed in Ar-O_2-Ar ambient could be related to the absence of nitrogen and/or hydrogen ions in which the release of oxygen ions during the incorporation of gallium ions into CeO_2 crystal lattice would either diffuse out from the PL or diffuse inward to react with Si surface, and thus, a less denser PL was formed. Although oxygen gas was being introduced during the dwelling stage for different postdeposition annealing ambient, the existence of nitrogen and/or hydrogen ions at the interface during annealing in N_2-O_2-N_2 and FG-O_2-FG ambient would possibly

Table 3: Thicknesses of $Ga_xCe_yO_z$ PL and SiO_2 IL extracted from XRR measurements for the investigated $Ga_xCe_yO_z$ PL. Total oxide thickness of the investigated $Ga_xCe_yO_z$ PL acquired from XRR and cross-sectional FESEM characterizations. The calculated k values using total oxide thickness from XRR measurement for the investigated $Ga_xCe_yO_z$ PL.

Annealing ambient	XRR: $Ga_xCe_yO_z$ PL thickness (nm)	XRR: SiO_2 IL thickness (nm)	XRR: total oxide thickness (nm)	Cross-sectional FESEM: total oxide thickness (nm)	k value
N_2-O_2-N_2	28.054 [51]	0.958 [51]	29.012 [51]	30.4	11.27 [51]
FG-O_2-FG	36.240	2.321	38.561	40.2	18.24
Ar-O_2-Ar	45.112	6.942	52.054	53.7	15.94

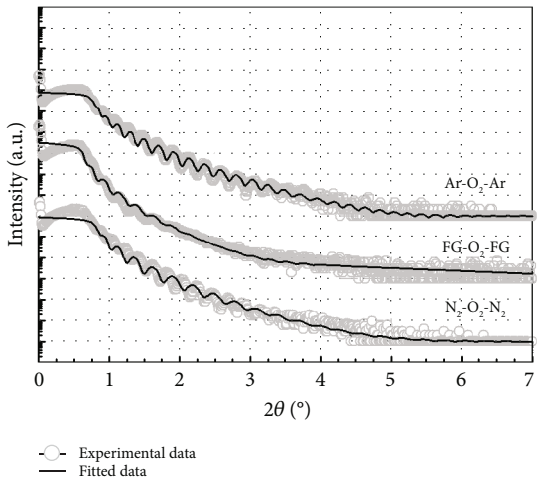

Figure 3: The experimental and fitted XRR result for $Ga_xCe_yO_z$ PL annealed in different ambient of N_2-O_2-N_2 [51], FG-O_2-FG, and Ar-O_2-Ar.

restrict the oxygen ions from reacting with Si surface, of which the unreacted oxygen ions would possibly diffuse outward and participate in the densification of the $Ga_xCe_yO_z$ PL. It was hypothesised that the acquisition of a lower E_a by the $Ga_xCe_yO_z$ PL annealed in FG-O_2-FG than that of N_2-O_2-N_2 ambient could be associated to the inclusion of additional hydrogen ions into the $Ga_xCe_yO_z$ lattice, which restricted the densification of this PL.

The Williamson-Hall (W-H) approach was adopted to estimate the microstrain (ε) and crystallite size (D) of the $Ga_xCe_yO_z$ PL, as represented by the subsequent equation [74]:

$$\frac{\beta_i \cos\theta_i}{\lambda} = \frac{1}{D} + \frac{4\varepsilon \sin\theta_i}{\lambda}, \tag{3}$$

where λ, θ_i, and β_i are X-ray wavelength, diffraction angle, and integral breadth (in radius 2θ) of the ith Bragg reflection positioned at $2\theta_i$. Figure 4 presents the typical W-H plot for $Ga_xCe_yO_z$ PL annealed in N_2-O_2-N_2 ambient. The slope and intercept from the constructed W-H plots were used to calculate the ε and D, respectively, for the investigated $Ga_xCe_yO_z$ PL annealed at 700°C in different ambient. Table 1 presents the estimated values of ε and D for the $Ga_xCe_yO_z$ PL. It was discerned that $Ga_xCe_yO_z$ PL annealed in both N_2-O_2-N_2 and FG-O_2-FG ambient have attained smaller D when compared with $Ga_xCe_yO_z$ PL annealed in Ar-O_2-Ar ambient. This observation could be associated to the existence of nitrogen and/or hydrogen ions in the $Ga_xCe_yO_z$ PL annealed in both N_2-O_2-N_2 and FG-O_2-FG ambient that have restricted the coalescence of crystallites. During annealing in Ar-O_2-Ar ambient, the absence of any additional nitrogen and/or hydrogen ions implies that the oxygen ions that diffused into the PL during dwelling stage could occupy the oxygen vacancies in the $Ga_xCe_yO_z$ lattice and assisted in the coalescence of crystallites, after which these oxygen ions were released to diffuse to the interface and react with the underlying Si surface. Therefore, the largest D was obtained for the $Ga_xCe_yO_z$ PL annealed in Ar-O_2-Ar ambient. Moreover, the attainment of the largest tensile ε in the $Ga_xCe_yO_z$ PL annealed in Ar-O_2-Ar ambient could be linked to the formation of oxygen vacancies in the PL. A reduction in tensile ε of the $Ga_xCe_yO_z$ PL annealed in N_2-O_2-N_2 ambient has suggested that the attachment of nitrogen ions to the oxygen vacancies would minimize the tensile ε induced on the $Ga_xCe_yO_z$ lattice. When FG-O_2-FG ambient was being employed during postdeposition annealing, the lessening in the release of adjacent oxygen ions due to the attachment of both hydrogen and nitrogen ions to the oxygen vacancies has reduced the concentration of oxygen vacancies being formed in $Ga_xCe_yO_z$ PL, and thus, the lowest tensile ε was obtained for this PL.

The determination of the preferred orientation for the $Ga_xCe_yO_z$ PL was accomplished by determining the coefficient of texture (T_{hkl}), which was formulated through the subsequent equation [75]:

$$T_{hkl} = \frac{I_m(hkl)}{I_o(hkl)} \div \frac{1}{n}\sum_{1}^{n}\frac{I_m(hkl)}{I_o(hkl)}, \tag{4}$$

where $I_o(hkl)$ is the intensity of the CeO_2 standard reference sample containing the same plane, $I_m(hkl)$ is the measured relative intensity of reflection from the (hkl) plane for $Ga_xCe_yO_z$ phase, and n is the number of $Ga_xCe_yO_z$ reflection peaks. Figure 5 shows the computed T_{hkl} values of the investigated $Ga_xCe_yO_z$ PL. A reference line of T_{hkl} value equal to 1 was also included in Figure 5 to denote the preferred growth in the specific plane. It was observed that $Ga_xCe_yO_z$ PL annealed in N_2-O_2-N_2 ambient has attained a preferred orientation along (200) plane. Nonetheless, the dominance of (200) plane has subsided with the emergence of (311) plane with T_{hkl} value larger than 1 when the $Ga_xCe_yO_z$ PL was annealed in FG-O_2-FG ambient. When Ar-O_2-Ar ambient was being employed during postdeposition annealing, it

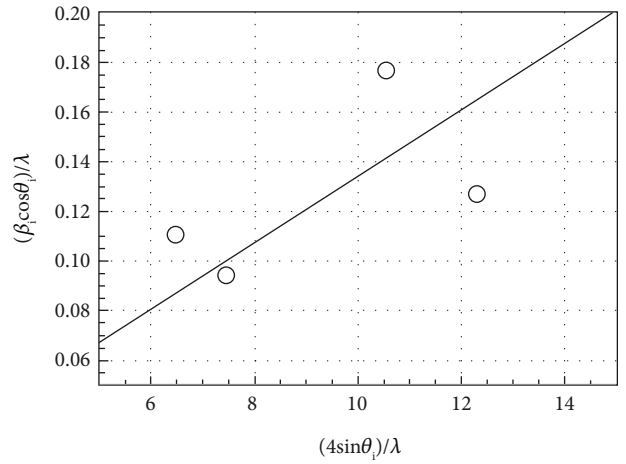

FIGURE 4: Typical W-H plot for $Ga_xCe_yO_z$ PL annealed in N_2-O_2-N_2 ambient.

was noticed that a mixed preferred orientation in (111) and (200) planes was attained with the (111) plane being more pronounced than (200) plane.

The UVVIS measurements in diffused reflectance mode enabled the determination of the direct (E^D) and indirect bandgap (E^{ID}) of the $Ga_xCe_yO_z$ PL by adopting the Kubelka-Munk (KM) function that could be represented by the subsequent equation [76]:

$$F(R) = \frac{(1-R)^2}{2R}, \tag{5}$$

where R is the diffused reflectance and the $F(R)$ function is multiplied by the photon energy $h\nu$ using 1/2 and 2 as the corresponding coefficients (n) for direct band and indirect band transitions, respectively. The direct E_g (E^D) and indirect E_g (E^{ID}) values of the investigated $Ga_xCe_yO_z$ PL were extracted via extrapolation on the linear region of $(F(R) \times h\nu)^n$ vs. $h\nu$ plot to zero (not shown). The extracted E^D and E^{ID} values for the investigated $Ga_xCe_yO_z$ PL are represented in Figure 6. It is noteworthy that the extracted values of E^D and E^{ID} from the investigated $Ga_xCe_yO_z$ PL, which ranged from 3.87 to 4.07 eV and 2.99 to 3.68 eV, respectively, were within the reported range of E^D (4.85 eV) and E^{ID} (4.66 eV) for Ga_2O_3, as well as E^D (3.12 eV) and E^{ID} (2.58 eV) for CeO_2 [73, 77]. This suggests that the Ga^{3+} cation has been successfully doped into the CeO_2 crystal lattice, resulting in the formation of ternary $Ga_xCe_yO_z$ phase. Among the investigated samples, the $Ga_xCe_yO_z$ PL annealed in N_2-O_2-N_2 ambient has attained the lowest E^D (3.87 eV) and E^{ID} (2.99 eV), which has denoted that the incorporation of nitrogen ions into the $Ga_xCe_yO_z$ lattice would trigger the narrowing of E^D and E^{ID}. Similar observation has also been reported for nitrogen-doped CeO_2 nanoparticles prepared through wet chemical route [78]. The enlargement of E^D and E^{ID} for $Ga_xCe_yO_z$ PL annealed in FG-O_2-FG ambient was in agreement with previous discussion that a higher concentration of nitrogen ions has diffused to the interface when compared with N_2-O_2-N_2 ambient, wherein the attachment of nitrogen ions to oxygen vacancies could be lower, leading to the acquisition of larger E^D (3.90 eV) and E^{ID} (3.10 eV). Nevertheless, $Ga_xCe_yO_z$ PL annealed in Ar-O_2-Ar ambient has attained the largest E^D (4.07 eV) and E^{ID} (3.68 eV) as no additional nitrogen and hydrogen ions were introduced into the $Ga_xCe_yO_z$ lattice.

The typical surface morphology of $Ga_xCe_yO_z$ PL annealed in Ar-O_2-Ar ambient that was characterized using FESEM technique is shown in Figure 7(d). It was revealed that all of the investigated $Ga_xCe_yO_z$ PL have acquired a smooth surface without visible cracks or voids. Additional assessment was conducted utilizing the AFM characterization, whereby the 3-dimensional surface topographies of the $Ga_xCe_yO_z$ PL were acquired at a scanning area of 10 μm^2 as presented in Figure 7. It was observed that smaller dimension protrusions with comparable height were uniformly formed throughout the surface of $Ga_xCe_yO_z$ PL annealed in a N_2-O_2-N_2 ambient (Figure 7(a)) leading to the attainment of the lowest root-mean-square (RMS) roughness of 0.793 nm. A substantial increment in RMS roughness to 2.080 nm was noticed when the $Ga_xCe_yO_z$ PL was annealed in FG-O_2-FG ambient, wherein a mixture of protrusions with large and small dimensions was formed throughout the surface of this PL (Figure 7(b)). It was observed that the surface of $Ga_xCe_yO_z$ PL annealed in Ar-O_2-Ar ambient was comprised of a section with extremely larger protrusion (Figure 7(c)), and thus, the highest RMS roughness of 2.580 nm was attained.

3.2. The Metal-Oxide-Semiconductor (MOS) Characteristics of the Al/$Ga_xCe_yO_z$/4H-SiC/Al MOS Capacitor. The bidirectional C-V curves measured at 1 MHz with applied voltage from -4 to +4 V for $Ga_xCe_yO_z$ PL subjected to different post-deposition annealing ambient are depicted in Figure 8. The estimation of dielectric constant (k) values has been carried out based on the subsequent equation [79]:

$$k = \frac{C_{ox} t_{ox}}{\varepsilon_o A}, \tag{6}$$

where C_{ox}, t_{ox}, ε_o, and A refer to the value of capacitance at accumulation level, total oxide thickness obtained from the XRR measurements (Table 3), free space permittivity, and metal contact area, respectively. The highest k value of 18.24 was perceived by the $Ga_xCe_yO_z$ PL annealed in FG-O_2-FG ambient, despite the formation of a thicker SiO_2 IL (2.32 nm) as evidenced by XRR measurement in comparison to the sample annealed in N_2-O_2-N_2 ambient (0.96 nm). It was reported previously that the formation of thicker SiO_2 IL possessing a lower k value of 3.90 would possibly contribute to the reduction of the overall k value of the investigated PL [78]. It was worth noting that the total capacitance (C_{tot}) of a MOS structure comprising of $Ga_xCe_yO_z$ PL and SiO_2 IL could be determined by the equation given below [80]:

$$\frac{1}{C_{tot}} = \frac{1}{C_{ox}} + \frac{1}{C_{IL}}, \tag{7}$$

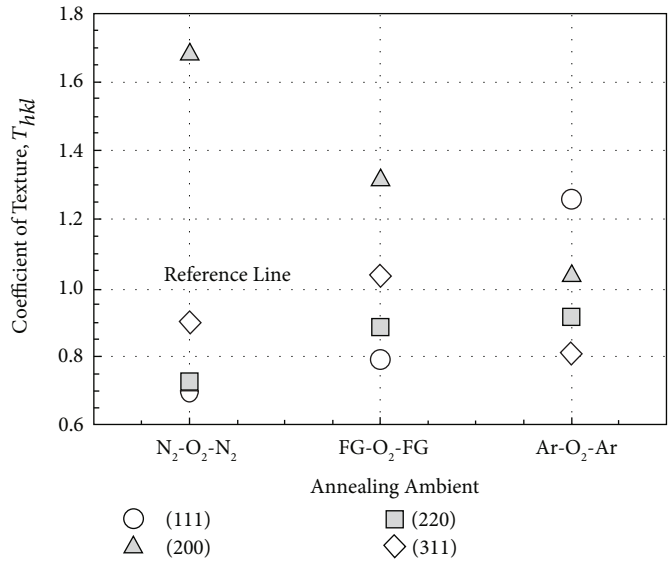

Figure 5: Coefficient of texture (T_{hkl}) for $Ga_xCe_yO_z$ PL subjected to different postdeposition annealing ambient of N_2-O_2-N_2 [51], FG-O_2-FG, and Ar-O_2-Ar at 700°C.

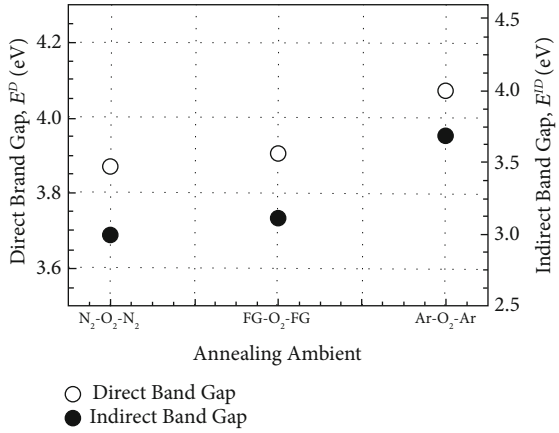

Figure 6: Direct and indirect band gap of $Ga_xCe_yO_z$ PL subjected to different postdeposition annealing ambient of N_2-O_2-N_2 [51], FG-O_2-FG, and Ar-O_2-Ar.

where C_{ox} and C_{IL} are referring to the capacitance of $Ga_xCe_yO_z$ PL and SiO_2 IL, respectively. Based on this equation, it was deduced that the value of capacitance in the accumulation level for the $Ga_xCe_yO_z$ PL annealed in FG-O_2-FG ambient could be dominated by the capacitance of $Ga_xCe_yO_z$ PL rather than the capacitance of SiO_2 IL. Similarly, it was also discovered that the k value of $Ga_xCe_yO_z$ PL annealed in Ar-O_2-Ar ambient ($k = 15.94$) was also controlled by the capacitance value of $Ga_xCe_yO_z$ PL, wherein the formation of thicker SiO_2 IL (6.94 nm) did not contribute to the acquisition of a higher k value when compared with $Ga_xCe_yO_z$ PL annealed in N_2-O_2-N_2 ambient ($k = 11.27$). A comparison between the k values obtained by $Ga_xCe_yO_z$ PL annealed in FG-O_2-FG ($k = 18.24$) and Ar-O_2-Ar ($k = 15.94$) ambient has disclosed that the formation of thicker SiO_2 IL would contribute to the reduction in k value, but the impact towards the k value could be less significant when compared to the thickness of $Ga_xCe_yO_z$ PL. Although $Ga_xCe_yO_z$ PL annealed in N_2-O_2-N_2 ambient has achieved a better densification than other PL, the reason of getting the lowest k value for this PL remains unknown. Nevertheless, it was determined in this work that the lowest k value (11.27) obtained by the $Ga_xCe_yO_z$ PL annealed in N_2-O_2-N_2 ambient at 700°C was higher than the CeO_2 passivation layers subjected to postdeposition annealing within the range of 600 ($k = 9.70$) to 800°C ($k = 6.30$) in N_2-O_2-N_2 ambient [8] and CeO_2 PL annealed at 700°C ($k = 8.00$) in oxygen ambient [81], suggesting that the incorporation of Ga^{3+} into CeO_2 lattice has contributed to the attainment of a larger k value.

The presented C-V curves for the investigated $Ga_xCe_yO_z$ PL in Figure 8 disclosed that negative flat band voltage shift (ΔV_{FB}) was attained for all samples denoting the existence of positively charged traps in the investigated $Ga_xCe_yO_z$ PL. It was ascertained that the largest negative ΔV_{FB} was perceived by the $Ga_xCe_yO_z$ PL annealed in Ar-O_2-Ar ambient designating the formation of the highest density of positively charged traps, which might be due to the formation of oxygen vacancies in the $Ga_xCe_yO_z$ PL. When FG-O_2-FG ambient were employed, the attachment of nitrogen and hydrogen ions to the oxygen vacancies simultaneously has hindered the released of adjacent oxygen ions from the $Ga_xCe_yO_z$ lattice, wherein a smaller negative ΔV_{FB} was perceived by this PL when compared with $Ga_xCe_yO_z$ PL annealed in Ar-O_2-Ar ambient. Moreover, the accumulation of negatively charged nitrogen ions at the interface would also compensate the positively charged oxygen vacancies in the $Ga_xCe_yO_z$ PL annealed in FG-O_2-FG ambient leading to the reduction in the overall positive charges in this PL. Furthermore, it was noticed that $Ga_xCe_yO_z$ PL annealed in N_2-O_2-N_2 ambient was comprised of the lowest density of positively charged traps due to the acquisition of the smallest negative ΔV_{FB}. Nevertheless, GIXRD measurement has

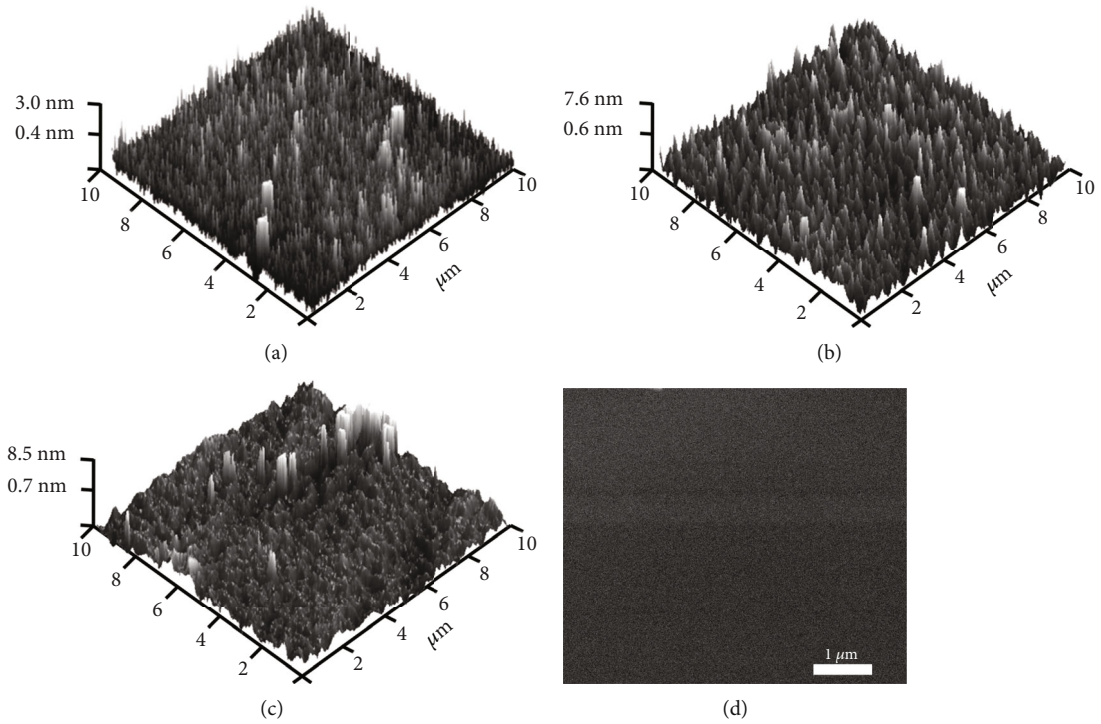

FIGURE 7: 3-dimensional surface topographies for $Ga_xCe_yO_z$ PL annealed in (a) N_2-O_2-N_2 [51], (b) Fg-O_2-Fg, and (c) Ar-O_2-Ar ambient. (d) The FESEM surface morphology of $Ga_xCe_yO_z$ PL annealed in Ar-O_2-Ar ambient.

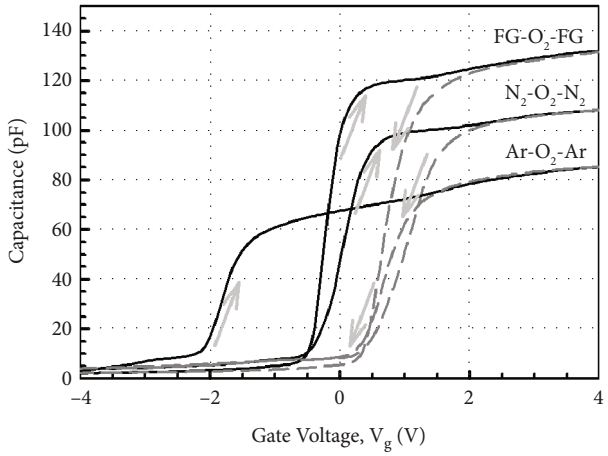

FIGURE 8: *C-V* curves for $Ga_xCe_yO_z$ PL annealed in different ambient of N_2-O_2-N_2 [51], FG-O_2-FG, and Ar-O_2-Ar.

disclosed the detection of $Ga_xCe_yO_z$ peaks demonstrating the largest variation when compared with standard CeO_2 sample for $Ga_xCe_yO_z$ PL annealed in N_2-O_2-N_2 ambient. This observation has implied the existence of more positively charged oxygen vacancies in the $Ga_xCe_yO_z$ PL annealed in N_2-O_2-N_2 ambient in which the adjacent oxygen ions in $Ga_xCe_yO_z$ lattice were released when nitrogen ions were being attached to the oxygen vacancies. In order to explain this discrepancy, it was postulated that the attachment of nitrogen ions to the oxygen vacancies during annealing in N_2-O_2-N_2 ambient would provide a smaller space in the $Ga_xCe_yO_z$ lattice for the subsequent nitrogen ions to diffuse through. As a result, these unattached negatively charged nitrogen ions could linger in the $Ga_xCe_yO_z$ lattice contributing to the acquisition of the lowest density of positively charged traps for $Ga_xCe_yO_z$ PL annealed in N_2-O_2-N_2 ambient. In order to further verify the density of positively charged traps in the investigated $Ga_xCe_yO_z$ PL, the following equation was used to calculate the effective oxide charge (Q_{eff}) of the investigated PL [82]:

$$Q_{eff} = \frac{\Delta V_{FB} C_{ox}}{qA}, \tag{8}$$

where q represents electronic charge. Figure 9 shows the calculated Q_{eff} values for the investigated $Ga_xCe_yO_z$ PL. In addition, it was also determined that the Q_{eff} values ranging from 1.83×10^{12} to 4.39×10^{12} cm^{-2} obtained by the $Ga_xCe_yO_z$ passivation layer annealed in different ambient of N_2-O_2-N_2, FG-O_2-FG, and Ar-O_2-Ar ambient were lower than the previously reported $Ta_xGd_yO_z$ (5.45×10^{12} cm^{-2}) [83] and HfO_2 (4.78×10^{12} cm^{-2}) [84] PL deposited on the Si substrate.

Further examination on the slow traps formed in the investigated $Ga_xCe_yO_z$ PL was calculated using the following slow trap density (STD) equation [85]:

$$\text{STD} = \frac{\Delta V C_{ox}}{qA}, \tag{9}$$

where ΔV is the difference between forward and reverse bias flat band voltage. Figure 9 presents the calculated STD of the investigated $Ga_xCe_yO_z$ PL. Among all the investigated $Ga_xCe_yO_z$ PL, the lowest STD was acquired by the

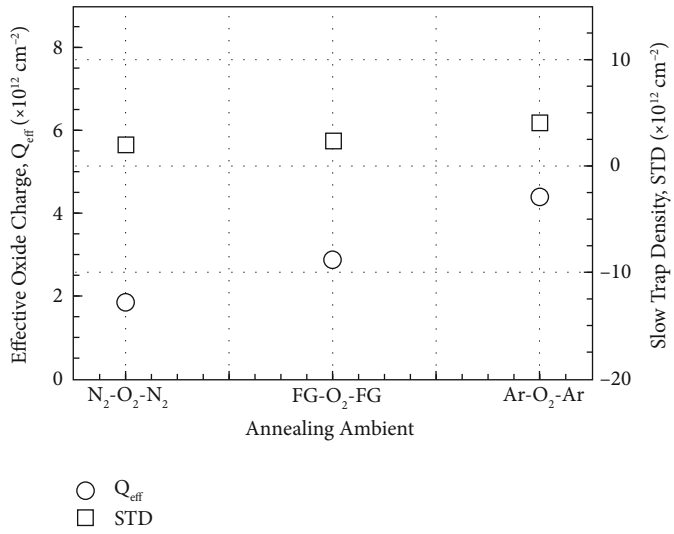

Figure 9: Q_{eff} and STD for $Ga_xCe_yO_z$ PL annealed in different ambient of N_2-O_2-N_2 [51], FG-O_2-FG, and Ar-O_2-Ar.

$Ga_xCe_yO_z$ PL annealed in N_2-O_2-N_2 ambient, which could be related to the negatively charged nitrogen ions accumulated at the interface. When the electrons were being injected during forward biased, these electrons would not be attracted to the negatively charged nitrogen ions accumulated at the interface, and thus, the probability of trapping the electrons would be lower leading to the attainment of the lowest STD for $Ga_xCe_yO_z$ PL annealed in N_2-O_2-N_2 ambient. A slight increment in STD was perceived when the $Ga_xCe_yO_z$ PL was annealed in FG-O_2-FG ambient, wherein the formation of weaker bonding between hydrogen ions and Si could be broken by the electrons during forward bias. Further increment in the forward bias would allow the subsequent injected electrons to be trapped by these positively charged Si dangling bonds, and these electrons would be detrapped during reverse biased. The nonexistence of nitrogen as well as hydrogen ions during annealing in Ar-O_2-Ar ambient would allow more electrons to be captured by the Si dangling bonds as well as the positively charged oxygen vacancies during forward bias. Thus, the highest STD was obtained by this PL as the defects were located nearer to the interface and could be potentially detrapped when reverse biased was being applied.

The interface quality between the investigated $Ga_xCe_yO_z$ PL and the Si substrate was analyzed using the Terman's method in which the interface trap density (D_{it}) could be determined based on the subsequent equation [86]:

$$D_{it} = \frac{C_{ox} d(\Delta V_g)}{qAd(\Phi_s)}, \quad (10)$$

where $\Delta V_g = V_g - V_{g(ideal)}$ is the voltage shift between the experimental (V_g) and the ideal curves and Φ_s is the surface potential at a specific gate voltage. Figure 10 shows the calculated D_{it} values as a function of energy trap level (E_c-E_t) for $Ga_xCe_yO_z$ PL subjected to different postdeposition annealing ambient. It was perceived that the best interface quality was attained by $Ga_xCe_yO_z$ PL annealed in N_2-O_2-N_2 ambient due to the acquisition of the lowest D_{it}. This could be an indication that the existence of nitrogen ions during annealing in N_2-O_2-N_2 ambient has succeeded in passivating the Si dangling bonds as well as forming an attachment with the oxygen vacancies located near to the interface between $Ga_xCe_yO_z$ PL and Si surface to reduce the D_{it} of the investigated PL. It was noticed that the D_{it} value of 4.21×10^{12} cm^{-2} eV^{-1} at 0.40 eV for the $Ga_xCe_yO_z$ PL annealed in N_2-O_2-N_2 ambient was comparable with Sc_2O_3 (4.80×10^{12} cm^{-2} eV^{-1} at 0.40 eV) [87] as well as HfAlO (4.00×10^{12} cm^{-2} eV^{-1} at 0.40 eV) [88] PL subjected to annealing in air and vacuum ambient, respectively. The acquisition of a higher D_{it} by the $Ga_xCe_yO_z$ PL annealed in FG-O_2-FG ambient could be related to the existence of unattached nitrogen ions that were accumulated at the interface in which these nitrogen dangling bonds would degrade the interface quality of the investigated PL [89, 90]. In addition, the presence of hydrogen ions with smaller ionic radius during annealing in FG-O_2-FG ambient would be able to diffuse faster to the interface to passivate the Si dangling bond in which more nitrogen dangling bonds could be formed leading to the attainment of a higher D_{it} when compared with $Ga_xCe_yO_z$ PL annealed in N_2-O_2-N_2 ambient. It was also discovered in this research work that nitrogen and/or hydrogen ions were effective in passivating the interface defects, wherein the employment of Ar-O_2-Ar ambient during postdeposition annealing has contributed to the acquisition of the highest D_{it}.

Besides, different frequencies spanning from 10 kHz to 1 MHz were employed to measure the C-V characteristics of the investigated $Ga_xCe_yO_z$ PL, and the obtained results were used to calculate interface state density (N_{ss}) based on high-low-frequency C-V method, conveyed by the subsequent equation [91]:

$$N_{ss} = \frac{1}{qA}\left[\left(\frac{1}{C_{LF}} - \frac{1}{C_{OX}}\right)^{-1} - \left(\frac{1}{C_{HF}} - \frac{1}{C_{OX}}\right)^{-1}\right], \quad (11)$$

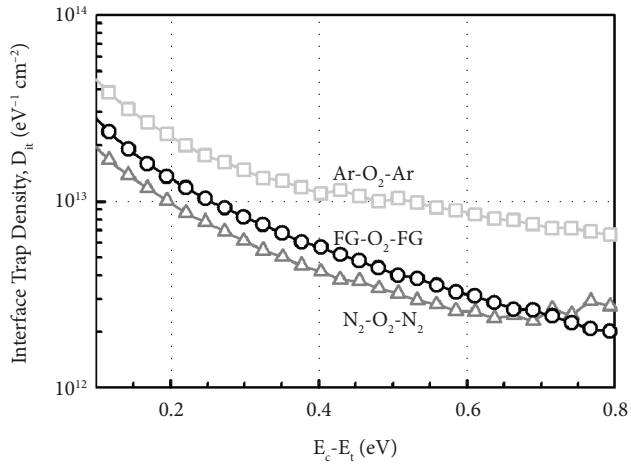

FIGURE 10: D_{it} as a function of E_c-E_t for the $Ga_xCe_yO_z$ PL subjected to annealing at 700°C in different ambient of N_2-O_2-N_2 [51], FG-O_2-FG, and Ar-O_2-Ar.

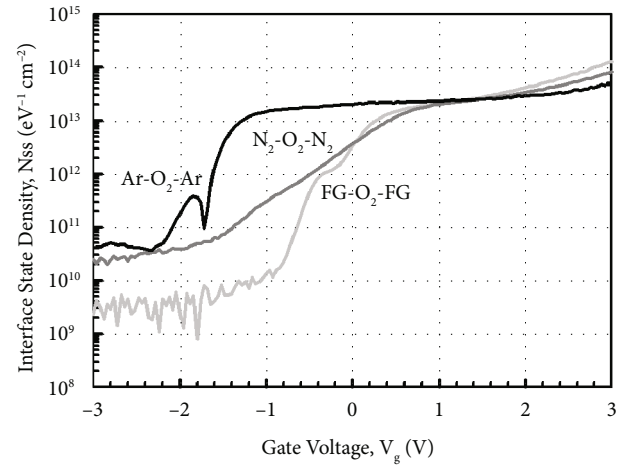

FIGURE 12: N_{ss} plot based on the high-low-frequency approach for the $Ga_xCe_yO_z$ PL annealed in different ambient of N_2-O_2-N_2 [51], FG-O_2-FG, and Ar-O_2-Ar.

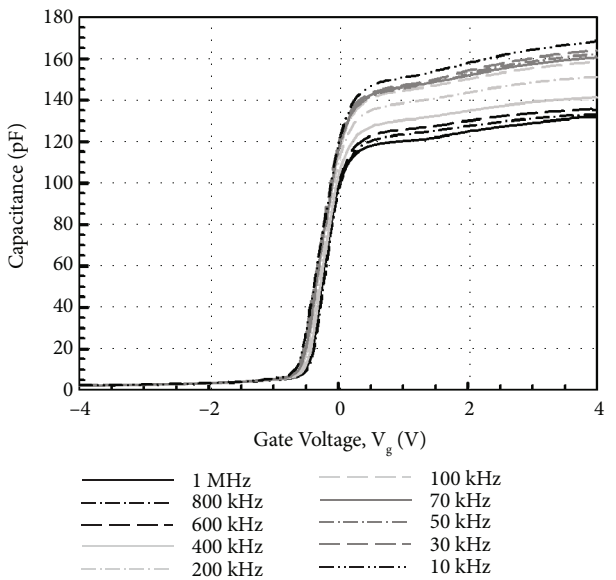

FIGURE 11: *C-V* measurements at different frequencies of 1 MHz to 10 kHz for $Ga_xCe_yO_z$ PL annealed in FG-O_2-FG ambient.

where C_{LF} is the lowest value of low-frequency (10 kHz) capacitance and C_{HF} is the highest value high-frequency (1 MHz) capacitance at voltage corresponding to C_{LF}. Figure 11 shows the typical different frequencies *C-V* curves measured for $Ga_xCe_yO_z$ PL annealed in FG-O_2-FG ambient. The calculated N_{ss} value with regard to V_g for the $Ga_xCe_yO_z$ PL is presented in Figure 12. In contrast, $Ga_xCe_yO_z$ PL annealed in FG-O_2-FG ambient at gate voltage below 0.05 V has procured lower N_{ss}, possibly due to the presence of fewer nitrogen dangling bonds serving as border traps. It was noticed that when the gate voltage was increased beyond 0.05 V, the N_{ss} for $Ga_xCe_yO_z$ PL annealed in FG-O_2-FG ambient was higher than $Ga_xCe_yO_z$ PL annealed in N_2-O_2-N_2 ambient, denoting that a higher concentration of border traps was located at a higher energy level. This observation has further supported the earlier explanation regarding the acquisition of a higher D_{it} using Terman's method for $Ga_xCe_yO_z$ PL annealed in FG-O_2-FG ambient, which has suggested that more nitrogen dangling bonds were formed at a higher energy level. The acquisition of the highest N_{ss} for $Ga_xCe_yO_z$ PL annealed in Ar-O_2-Ar ambient was in agreement with the Terman's method, wherein the nonexistence of nitrogen and/or hydrogen ions during annealing was not able to passivate the oxygen vacancies located nearer to the interface as well as Si dangling bonds.

Figure 13 illustrates the leakage current density-electric field (*J* - *E*) characteristics of the $Ga_xCe_yO_z$ PL annealed at 700°C in different ambient. At *E* below 0.5 MV/cm, $Ga_xCe_yO_z$ PL annealed in FG-O_2-FG ambient has demonstrated a lower *J* due to the existence of a higher concentration of border traps located at a lower trap energy level in which high-low-frequency *C-V* measurement has revealed the acquisition of a lower N_{ss} at gate voltage below 0.05 V. A deterioration in *J* was perceived as the *E* was enhanced to the region of 0.5 to 2.0 MV/cm for the $Ga_xCe_yO_z$ PL annealed in FG-O_2-FG ambient, which was due to the presence of a higher density of border traps at a higher gate voltage of 0.05 V as well as a higher D_{it}. Nonetheless, a sudden improvement in *J* at *E* within the region of 2.0 to 3.0 MV/cm for the $Ga_xCe_yO_z$ PL annealed in FG-O_2-FG ambient was due to the formation of thicker SiO_2 IL and the highest *k* value when compared with $Ga_xCe_yO_z$ PL annealed in N_2-O_2-N_2 ambient. Although $Ga_xCe_yO_z$ PL annealed in N_2-O_2-N_2 ambient has attained the lowest *k* value, this PL was able to withstand the highest electric breakdown field of ~4.95 MV/cm that could be potentially due to the acquisition of the lowest Q_{eff}, STD, and D_{it}. It was revealed that the acquired electric breakdown field (E_B) of 4.95 MV/cm for the $Ga_xCe_yO_z$ PL annealed in N_2-O_2-N_2 ambient was better when compared with E_B of bilayer HfO_2/SiO_2 (3.90 MV/cm) PL [92]. Moreover, the attained leakage current density of 2.57×10^{-6} A/cm^{-2} at 1 MV/cm for the $Ga_xCe_yO_z$ PL annealed in N_2-O_2-N_2 ambient was lower than the magnetron sputtered ErAlO PL on Si substrate (8.40×10^{-5} A/cm^2 at

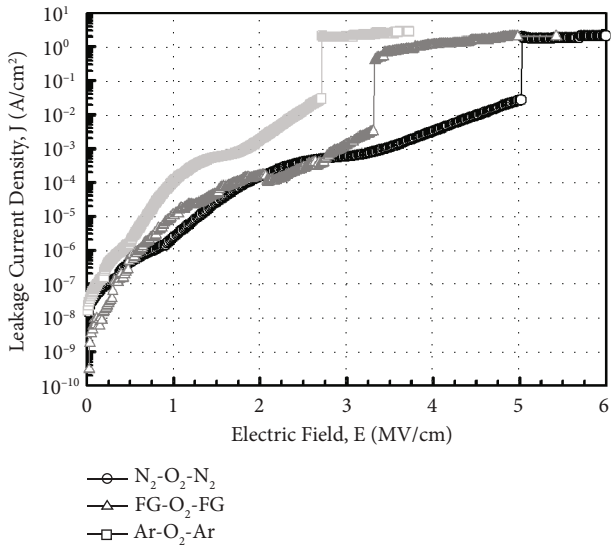

FIGURE 13: J - E characteristics of $Ga_xCe_yO_z$ PL annealed in different ambient of N_2-O_2-N_2 [51], FG-O_2-FG, and Ar-O_2-Ar.

1 MV/cm) [80]. It was discerned that $Ga_xCe_yO_z$ PL annealed in Ar-O_2-Ar ambient has demonstrated the lowest electric breakdown field (~2.71 MV/cm) due to the formation of the thickest SiO_2 IL as well as the less dense $Ga_xCe_yO_z$ PL, resulting in a poor J - E characteristic. It was postulated that the formation of the thickest SiO_2 IL during annealing in Ar-O_2-Ar ambient would assist in enhancing the electric breakdown field of this PL with the requirement that a high-quality SiO_2 IL was formed. However, the attainment of the poorest J - E characteristic by this $Ga_xCe_yO_z$ PL annealed in Ar-O_2-Ar ambient has suggested that a low quality of SiO_2 IL was formed contributing to a degradation in E_B of this PL.

4. Conclusion

A comparison study among $Ga_xCe_yO_z$ PL annealed in different ambient (N_2-O_2-N_2, FG-O_2-FG, and Ar-O_2-Ar) was carried out systematically. Hydrogen present in the FG-O_2-FG ambient would attach to oxygen vacancies in the $Ga_xCe_yO_z$ PL, stimulating diffusion of nitrogen from the ambient to the $Ga_xCe_yO_z$/Si interface. Effectiveness of nitrogen and/or hydrogen in reducing the formation of SiO_2 IL was reported. The extracted E^D and E^{ID} values (3.87 to 4.07 and 2.99 to 3.68 eV, respectively) were within the range of reported values for CeO_2 and Ga_2O_3, which further reinstated the formation of the ternary $Ga_xCe_yO_z$ phase. The $Ga_xCe_yO_z$ PL annealed in FG-O_2-FG ambient possessed the largest k value of 18.24, followed by the samples annealed Ar-O_2-Ar (15.94) and N_2-O_2-N_2 (11.27) ambient. It was revealed that N_2-O_2-N_2 ambient was effective in passivating Si dangling bonds and oxygen vacancies in addition to the accumulation of nitrogen at the interface, which resulted in the acquisition of a lower D_{it}, Q_{eff}, and STD. However, a higher concentration of unattached nitrogen in the $Ga_xCe_yO_z$ PL annealed in FG-O_2-FG has degraded the interface quality when compared with the sample annealed in N_2-O_2-N_2 ambient. Moreover, annealing in Ar-O_2-Ar ambient has led to the acquisition of the lowest E_B (2.71 MV/cm) due to the attainment of the highest Q_{eff}, STD, D_{it}, and N_{ss}. Hence, it was perceived that a low quality of SiO_2 IL was formed during annealing in Ar-O_2-Ar ambient contributing to the attainment of the lowest E_B. Although the $Ga_xCe_yO_z$ PL annealed in N_2-O_2-N_2 ambient has a lower k value than other samples, the acquisition of a high E_B of 4.95 MV/cm could be associated to the acquisition of low Q_{eff}, STD, N_{ss}, and D_{it}, which have supported its compatibility as a potential candidate as a high-k PL for future Si-based MOS applications.

Data Availability

The raw/processed data required to reproduce these findings cannot be shared at this time as the data also forms part of an ongoing study.

Conflicts of Interest

The authors declare that they have no conflicts of interest.

Acknowledgments

The authors would like to acknowledge the financial support from the Ministry of Higher Education Malaysia for Fundamental Research Grant Scheme (FRGS) with Project Code FRGS/1/2023/STG05/USM/02/8.

References

[1] J. Ajayan, D. Nirmal, and T. Shubham, "Nanosheet field effect transistors-a next generation device to keep Moore's law alive: an intensive study," *Microelectronics Journal*, vol. 114, article 105141, 2021.

[2] J. C. Ranuárez, M. J. Deen, and C. H. Chen, "A review of gate tunneling current in MOS devices," *Microelectronics and Reliability*, vol. 46, no. 12, pp. 1939–1956, 2006.

[3] E. Y. Wu, J. Suñé, W. Lai, A. Vayshenker, E. Nowak, and D. Harmon, "Critical reliability challenges in scaling SiO_2-based dielectric to its limit," *Microelectronics Reliability*, vol. 43, no. 8, pp. 1175–1184, 2003.

[4] D. G. Schlom, S. Guha, and S. Datta, "Gate oxides beyond SiO_2," *MRS Bulletin*, vol. 33, no. 11, pp. 1017–1025, 2008.

[5] D. Sánchez Ahumada, "In-situ low-temperature synthesis of PS-ZrO_2 hybrid films and their characterization for high-k gate dielectric application," *Progress in Organic Coating*, vol. 154, article 106188, 2021.

[6] A. Razavieh, P. Zeitzoff, and E. J. Nowak, "Challenges and limitations of CMOS scaling for FinFET and beyond architectures," *IEEE Transactions on Nanotechnology*, vol. 18, pp. 999–1004, 2019.

[7] Y. Peng and X. Wenwu, "Memory behavior of an Al_2O_3 gate dielectric non-volatile field-effect transistor," *IEEE Electron Device Letters*, vol. 41, no. 9, pp. 1340–1343, 2020.

[8] K. M. Abdul Shekkeer, K. Y. Cheong, and H. J. Quah, "Effects of post-deposition annealing of cerium oxide passivation layer in nitrogen-oxygen-nitrogen ambient," *International Journal of Energy Research*, vol. 46, no. 11, pp. 14814–14826, 2022.

[9] T. M. Pan and W. S. Huang, "Physical and electrical characteristics of a high-k Yb_2O_3 gate dielectric," *Applied Surface Science*, vol. 255, no. 9, pp. 4979–4982, 2009.

[10] J. B. Seon, N. K. Cho, G. Yoo, Y. S. Kim, and K. Char, "Solution-processed amorphous ZrO_2 gate dielectric films synthesized by a non-hydrolytic sol-gel route," *RSC Advances*, vol. 8, no. 68, pp. 39115–39119, 2018.

[11] M. Ding and X. Liu, "Damage effect of hafnium oxide gate dielectric based metal-oxide-semiconductor structure under gamma-ray irradiation," *AIP Advances*, vol. 11, no. 6, article 065304, 2021.

[12] T. M. Pan, J. der Lee, W. H. Shu, and T. te Chen, "Structural and electrical properties of neodymium oxide high-k gate dielectrics," *Applied Physics Letters*, vol. 89, no. 23, article 232908, 2006.

[13] J. B. Cheng, A. Li, Q. Y. Shao et al., "Growth and characteristics of La_2O_3 gate dielectric prepared by low pressure metalorganic chemical vapor deposition," *Applied Surface Science*, vol. 233, no. 1-4, pp. 91–98, 2004.

[14] L. Yan, C. M. Lopez, R. P. Shrestha, E. A. Irene, A. A. Suvorova, and M. Saunders, "Magnesium oxide as a candidate high-κ gate dielectric," *Applied Physics Letters*, vol. 88, no. 14, article 142901, 2006.

[15] J. J. Wang, Z. B. Fang, T. Ji, W. Y. Ren, Y. Y. Zhu, and G. He, "Band offsets of epitaxial Tm_2O_3 high-k dielectric films on Si substrates by X-ray photoelectron spectroscopy," *Applied Surface Science*, vol. 258, no. 16, pp. 6107–6110, 2012.

[16] K. Y. Tan, P. H. Megat Abdul Hedei, A. R. Mohd Zabidi et al., "Comparative studies of metal-organic decomposed $Ga_xCe_yO_z$ and CeO_2 based functional MOS capacitor," *International Journal of Energy Research*, vol. 45, no. 12, pp. 18257–18261, 2021.

[17] T. Yu, B. Lim, and Y. Xia, "Aqueous-phase synthesis of single-crystal ceria nanosheets," *Angewandte Chemie*, vol. 122, no. 26, pp. 4586–4589, 2010.

[18] F. C. Chiu and S. H. Chang, "Electrical analyses of charge trapping and stress-induced leakage current in CeO_2 gate dielectric," *Journal of the Chinese Institute of Engineers*, vol. 37, no. 3, pp. 407–412, 2014.

[19] F. C. Chiu, S. Y. Chen, C. H. Chen, H. W. Chen, H. S. Huang, and H. L. Hwang, "Interfacial and electrical characterization in metal–oxide–semiconductor field-effect transistors with CeO_2 gate dielectric," *Japanese Journal of Applied Physics*, vol. 48, no. 4S, article 04C014, 2009.

[20] F. C. Chiu and C. M. Lai, "Optical and electrical characterizations of cerium oxide thin films," *Journal of Physics D: Applied Physics*, vol. 43, no. 7, article 075104, 2010.

[21] A. Siddiqui, R. Y. Khosa, and M. Usman, "High-k dielectrics for 4H-silicon carbide: present status and future perspectives," *Journal of Materials Chemistry C*, vol. 9, no. 15, pp. 5055–5081, 2021.

[22] J. C. Wang, Y. P. Hung, C. L. Lee, and T. F. Lei, "Improved characteristics of ultrathin CeO_2 by using postnitridation annealing," *Journal of the Electrochemical Society*, vol. 151, no. 2, 2004.

[23] K. D. Kumar, Y. A. Kumar, T. Ramachandran, A. A. Al-Kahtani, and M. Kang, "Cactus-Like Ni-Co/$CoMn_2O_4$ composites on Ni foam: unveiling the potential for advanced electrochemical materials for pseudocapacitors," *Materials Science and Engineering: B*, vol. 296, article 116715, 2023.

[24] Y. A. Kumar, C. J. Raorane, H. H. Hegazy, T. Ramachandran, S. C. Kim, and M. Moniruzzaman, "2D MXene-based supercapacitors: a promising path towards high-performance energy storage," *Journal of Energy Storage*, vol. 72, article 108433, 2023.

[25] Y. Ling, X. Liao, and C. Liu, "Poly(l-lactide-co-caprolactone)/tussah silk fibroin nanofiber vascular scaffolds with small diameter fabricated by core-spun electrospinning technology," *Journal of Materials Science*, vol. 55, no. 16, pp. 7106–7119, 2020.

[26] L. Zhang, L. Sun, Q. Meng et al., "Strain-engineered formation, migration, and electronic properties of polaronic defects in CeO_2," *Physica Status Solidi (b)*, vol. 258, no. 6, article 2100020, 2021.

[27] D. Mamedov and S. Z. Karazhanov, "Doping-induced modulation of electronic, optical and wetting properties of CeO_2," *Journal of Physics and Chemistry of Solids*, vol. 168, article 110820, 2022.

[28] M. Machida, Y. Murata, K. Kishikawa, D. Zhang, and K. Ikeue, "On the reasons for high activity of CeO_2 catalyst for soot oxidation," *Chemistry of Materials*, vol. 20, no. 13, pp. 4489–4494, 2008.

[29] M. G. Brik, C. G. Ma, M. Piasecki, and A. Suchocki, "Locating impurity and defect levels in the host band gap by first-principles calculations: pure and Ce^{3+}-doped $YAlO_3$," *Optical Materials*, vol. 113, article 110843, 2021.

[30] B. Choudhury and A. Choudhury, "Ce^{3+} and oxygen vacancy mediated tuning of structural and optical properties of CeO_2 nanoparticles," *Materials Chemistry and Physics*, vol. 131, no. 3, pp. 666–671, 2012.

[31] Y. C. Chen, K. B. Chen, C. S. Lee, and M. C. Lin, "Direct synthesis of Zr-doped ceria nanotubes," *Journal of Physical Chemistry C*, vol. 113, no. 13, pp. 5031–5034, 2009.

[32] W. Qin, L. Xu, J. Song, R. Xing, and H. Song, "Highly enhanced gas sensing properties of porous SnO_2-CeO_2 composite nanofibers prepared by electrospinning," *Sensors and Actuators B: Chemical*, vol. 185, pp. 231–237, 2013.

[33] E. Rocchini, A. Trovarelli, J. Llorca et al., "Relationships between structural/morphological modifications and oxygen storage-redox behavior of silica-doped ceria," *Journal of Catalysis*, vol. 194, no. 2, pp. 461–478, 2000.

[34] M. Fu, L. Wei, Y. Li, X. Zhou, S. Hao, and Y. Li, "Surface charge tuning of ceria particles by titanium doping: towards significantly improved polishing performance," *Solid State Sciences*, vol. 11, no. 12, pp. 2133–2137, 2009.

[35] J. R. Scheffe, R. Jacot, G. R. Patzke, and A. Steinfeld, "Synthesis, characterization, and thermochemical redox performance of Hf^{4+}, Zr^{4+}, and Sc^{3+} doped ceria for splitting CO_2," *Journal of Physical Chemistry C*, vol. 117, no. 46, pp. 24104–24114, 2013.

[36] D. A. Andersson, S. I. Simak, N. V. Skorodumova, I. A. Abrikosov, and B. Johansson, "Theoretical study of CeO_2 doped with tetravalent ions," *Physical Review B*, vol. 76, no. 17, article 174119, 2007.

[37] Y. Tang, H. Zhang, L. Cui et al., "First-principles investigation on redox properties of M-dopedCeO2(M=Mn,Pr,Sn,Zr)," *Physical Review B*, vol. 82, no. 12, article 125104, 2010.

[38] G. Manibalan, G. Murugadoss, R. Thangamuthu, M. R. Kumar, and R. M. Kumar, "Facile synthesis of CeO_2-SnO_2 nanocomposite for electrochemical determination of L-cysteine," *Journal of Alloys and Compounds*, vol. 792, pp. 1150–1161, 2019.

[39] P. R. L. Keating, D. O. Scanlon, and G. W. Watson, "Computational testing of trivalent dopants in CeO_2 for improved high-κ dielectric behaviour," *Journal of Materials Chemistry C*, vol. 1, no. 6, pp. 1093–1098, 2013.

[40] N. Shehata, K. Meehan, M. Hudait, and N. Jain, "Control of oxygen vacancies and Ce^{+3} concentrations in doped ceria nanoparticles via the selection of lanthanide element," *Journal of Nanoparticle Research*, vol. 14, no. 10, pp. 1–10, 2012.

[41] L. Minervini, M. O. Zacate, and R. W. Grimes, "Defect cluster formation in M_2O_3-doped CeO_2," *Solid State Ionics*, vol. 116, no. 3-4, pp. 339–349, 1999.

[42] R. Gerhardt Anderson and A. S. Nowick, "Ionic conductivity of CeO_2 with trivalent dopants of different ionic radii," *Solid State Ionics*, vol. 5, pp. 547–550, 1981.

[43] M. E. Kilic, J. H. Lee, and K. R. Lee, "Oxygen ion transport in doped ceria: effect of vacancy trapping," *Journal of Materials Chemistry A*, vol. 9, no. 24, pp. 13883–13889, 2021.

[44] R. Gerhardt, W. Lee, and A. S. Nowick, "Anelastic and dielectric relaxation of Scandia-doped ceria," *Journal of Physics and Chemistry of Solids*, vol. 48, no. 6, pp. 563–569, 1987.

[45] K. M. A. Shekkeer, K. Y. Cheong, and H. J. Quah, "Growth of quaternary $Ga_xCe_{1-x}O_yN_z$ passivation layer for silicon based metal-oxide-semiconductor capacitor," *Materials Chemistry and Physics*, vol. 290, article 126549, 2022.

[46] S. J. Patwe and A. K. Tyagi, "Solubility of Ce^{4+} and Sr^{2+} in the pyrochlore lattice of $Gd_2Zr_2O_7$ for simulation of Pu and alkaline earth metal," *Ceramics International*, vol. 32, no. 5, pp. 545–548, 2006.

[47] Z. P. Li, T. Mori, J. Zou, and J. Drennan, "Defects clustering and ordering in di- and trivalently doped ceria," *Materials Research Bulletin*, vol. 48, no. 2, pp. 807–812, 2013.

[48] A. A. Dakhel, "Investigation of opto-dielectric properties of Ti-doped Ga_2O_3 thin films," *Solid State Sciences*, vol. 20, pp. 54–58, 2013.

[49] T. Onuma, S. Fujioka, T. Yamaguchi et al., "Correlation between blue luminescence intensity and resistivity in β-Ga_2O_3 single crystals," *Applied Physics Letters*, vol. 103, no. 4, article 041910, 2013.

[50] X. Li, H. Lu, and J. Yang, "Chemical, optical, and electrical characterization of Ga_2O_3 thin films grown by plasma-enhanced atomic layer deposition," *Current Applied Physics*, vol. 19, no. 2, pp. 72–81, 2019.

[51] K. M. Abdul Shekkeer, K. Y. Cheong, and H. J. Quah, "Alteration in growth temperatures of metal-organic decomposed $Ga_xCe_{1-x}O_yN_z$ passivation layer in nitrogen/oxygen/nitrogen ambient," *Ceramics International*, vol. 49, no. 9, pp. 14760–14770, 2023.

[52] Y. L. Yang, C. Y. Cheng, and W. K. Yeh, "Reliability improvement of 28-nm High-*k*/metal gate-last MOSFET using appropriate oxygen annealing," *IEEE Electron Device Letters*, vol. 33, no. 8, pp. 1183–1185, 2012.

[53] S. Y. Tan, "Control of interface traps in HfO_2 gate dielectric on silicon," *Journal of Electronic Materials*, vol. 39, no. 11, pp. 2435–2440, 2010.

[54] R. E. Stahlbush, H. L. Hughes, and W. A. Krull, "Reduction of charge trappings and electron tunneling in SIMOX by supplemental implantation of oxygen," *IEEE Transactions on Nuclear Science*, vol. 40, no. 6, pp. 1740–1747, 1993.

[55] T. Dimitrova, K. Arshak, and E. Atanassova, "Crystallization effects in oxygen annealed Ta_2O_5 thin films on Si," *Thin Solid Films*, vol. 381, no. 1, pp. 31–38, 2001.

[56] E. Atanassova, N. Novkovski, A. Paskaleva, and M. Pecovska-Gjorgjevich, "Oxygen annealing modification of conduction mechanism in thin rf sputtered Ta_2O_5 on Si," *Solid State Electronics*, vol. 46, no. 11, pp. 1887–1898, 2002.

[57] H. Yang, Y. Q. Wang, H. Wang, and Q. X. Jia, "Oxygen concentration and its effect on the leakage current in $BiFeO_3$ thin films," *Applied Physics Letters*, vol. 96, no. 1, article 012909, 2010.

[58] K. Tagui, K. Nakamura, M. Ogawa, K. Saito, and S. Suzuki, "The Electrical Property of CeO_2 Films Deposited by MOCVD on Si(100)," *Electrochemical and Solid-State Letters*, vol. 10, no. 7, article D73, 2007.

[59] L. Tye, N. A. El-Masry, T. Chikyow, P. McLarty, and S. M. Bedair, "Electrical characteristics of epitaxial CeO_2 on Si(111)," *Applied Physics Letters*, vol. 65, no. 24, pp. 3081–3083, 1994.

[60] M. Qu, C. H. Chang, T. Meng, Q. Zhang, P. T. Liu, and H. P. D. Shieh, "Stability study of indium tungsten oxide thin-film transistors annealed under various ambient conditions," *Physica Status Solidi (a)*, vol. 214, no. 2, article 1600465, 2017.

[61] Y.-S. Lin, R. Puthenkovilakam, J. P. Chang et al., "Interfacial properties of ZrO_2 on silicon," *Journal of Applied Physics*, vol. 93, no. 10, pp. 5945–5952, 2003.

[62] H. D. Kim, S.-W. Jeong, M. T. You, and Y. Roh, "Effects of annealing gas (N_2, N_2O, O_2) on the characteristics of $ZrSi_xO_y/ZrO_2$ high-k gate oxide in MOS devices," *Thin Solid Films*, vol. 515, no. 2, pp. 522–525, 2006.

[63] A. S. Zoolfakar, "Study of zirconium dioxide (ZrO_2) dielectric charges," *Materials Research Innovations*, vol. 13, no. 3, pp. 161–164, 2009.

[64] E. Simoen, A. Rothschild, B. Vermang, J. Poortmans, and R. Mertens, "Impact of forming gas annealing and firing on the Al_2O_3/p-Si interface state spectrum," *Electrochemical and Solid-State Letters*, vol. 14, no. 9, pp. H362–H364, 2011.

[65] N. Yamada and H. Yamada-Kaneta, "Drastic improvements of gate oxide reliability by argon annealing compared with hydrogen annealing," *Journal of the Electrochemical Society*, vol. 145, no. 10, pp. 3628–3631, 1998.

[66] H. J. Quah and K. Y. Cheong, "Deposition and post-deposition annealing of thin Y_2O_3 film on n-type Si in argon ambient," *Materials Chemistry and Physics*, vol. 130, no. 3, pp. 1007–1015, 2011.

[67] Y. A. Kumar, G. Koyyada, T. Ramachandran et al., "Carbon materials as a conductive skeleton for supercapacitor electrode applications: a review," *Nanomaterials*, vol. 13, no. 6, p. 1049, 2023.

[68] Y. A. Kumar, G. Koyyada, T. Ramachandran et al., "Recent advancement in quantum dot-based materials for energy storage applications: a review," *Dalton Transactions*, vol. 52, no. 25, pp. 8580–8600, 2023.

[69] K. Y. Tan and H. J. Quah, "Growth of metal-organic decomposed ternary $Ga_xCe_yO_z$ films by nitrogen-infused wet oxidation for metal-oxide-semiconductor capacitor," *International Journal of Energy Research*, vol. 46, no. 5, pp. 5756–5770, 2022.

[70] V. Ramasamy and G. Vijayalakshmi, "Effect of Zn doping on structural, optical and thermal properties of CeO_2 nanoparticles," *Superlattices and Microstructures*, vol. 85, pp. 510–521, 2015.

[71] K. J. Patel, C. J. Panchal, M. S. Desai, and P. K. Mehta, "An investigation of the insertion of the cations H^+, Na^+, K^+ on the electrochromic properties of the thermally evaporated WO_3 thin films grown at different substrate temperatures," *Materials Chemistry and Physics*, vol. 124, no. 1, pp. 884–890, 2010.

[72] J. Chen, S. Shen, P. Wu, and L. Guo, "Nitrogen-doped CeO_x nanoparticles modified graphitic carbon nitride for enhanced

photocatalytic hydrogen production," *Green Chemistry*, vol. 17, no. 1, pp. 509–517, 2015.

[73] R. S. Muller and T. I. Theodore, *Device electronics for integrated circuits*, John Wiley & Sons, 2002.

[74] M. Gupta, A. Kumar, A. Sagdeo, and P. R. Sagdeo, "Doping-induced combined fano and phonon confinement effect in La-doped CeO_2: Raman spectroscopy analysis," *Journal of Physical Chemistry C*, vol. 125, no. 4, pp. 2648–2658, 2021.

[75] R. Suresh, V. Ponnuswamy, R. Mariappan, and N. Senthil Kumar, "Influence of substrate temperature on the properties of CeO_2 thin films by simple nebulizer spray pyrolysis technique," *Ceramics International*, vol. 40, no. 1, pp. 437–445, 2014.

[76] P. K. Sane, S. Tambat, S. Sontakke, and P. Nemade, "Visible light removal of reactive dyes using CeO_2 synthesized by precipitation," *Journal of Environmental Chemical Engineering*, vol. 6, no. 4, pp. 4476–4489, 2018.

[77] B. Tatar, E. D. Sam, K. Kutlu, and M. Ürgen, "Synthesis and optical properties of CeO_2 nanocrystalline films grown by pulsed electron beam deposition," *Journal of Materials Science*, vol. 43, no. 15, pp. 5102–5108, 2008.

[78] C. Mao, Y. Zhao, X. Qiu, J. Zhu, and C. Burda, "Synthesis, characterization and computational study of nitrogen-doped CeO_2 nanoparticles with visible-light activity," *Physical Chemistry Chemical Physics*, vol. 10, no. 36, pp. 5633–5638, 2008.

[79] M. M. Islam, J. K. Saha, and R. N. Bukke, "Solution-processed La alloyed ZrO_x high-*k* dielectric for high-performance ZnO thin-film transistors," *IEEE Electron Device Letters*, vol. 41, pp. 1021–1024, 2020.

[80] Y. Y. Zhu, Z. B. Fang, and Y. S. Tan, "Structural and electrical characteristics of amorphous ErAlO gate dielectric films," *Chinese Physics Letters*, vol. 29, no. 8, article 087701, 2012.

[81] H. Fukuda, M. Miura, S. Sakuma, and S. Nomura, "Structural and electrical properties of crystalline CeO_2 films formed by metalorganic decomposition," *Japanese Journal of Applied Physics*, vol. 37, no. 7R, pp. 4158–4161, 1998.

[82] R. Pascu, C. Romanitan, P. Varasteanu, and M. Kusko, "A reliable technology for advanced SiC-MOS devices based on fabrication of high quality silicon oxide layers by converting a-Si," *IEEE Journal of the Electron Devices Society*, vol. 7, pp. 158–167, 2019.

[83] S. Li, Y. Wu, G. Li et al., "Ta-doped modified Gd_2O_3 film for a novel high k gate dielectric," *Journal of Materials Science*, vol. 35, pp. 2305–2311, 2019.

[84] J. Gao, G. He, J. W. Zhang, B. Deng, and Y. M. Liu, "Annealing temperature modulated interfacial chemistry and electrical characteristics of sputtering-derived HfO_2/Si gate stack," *Journal of Alloys and Compounds*, vol. 647, pp. 322–330, 2015.

[85] H. J. Quah, Z. Hassan, and W. F. Lim, "Passivation of silicon substrate using two-step grown ternary aluminium doped zirconium oxide," *Applied Surface Science*, vol. 493, pp. 411–422, 2019.

[86] D. K. Schroder, *Semiconductor Material and Device Characterization*, John Wiley & Sons, Inc., 2005.

[87] A. Belosludtsev, Y. Yakimov, R. Mroczyński et al., "Effect of annealing on optical, mechanical, electrical properties and structure of scandium oxide films," *Physica Status Solidi (a)*, vol. 216, no. 18, pp. 1900122–1900129, 2019.

[88] J. Gao, G. He, J. Zhang, X. Chen, P. Jin, and Z. Sun, "Annealing temperature dependent electrical properties and leakage current transport mechanisms in atomic layer deposition-derived Al_2O_3-incorporated HfO_2/Si gate stack," *Journal of Nanoscience and Nanotechnology*, vol. 16, no. 8, pp. 8075–8082, 2016.

[89] E. C. Lee, "Nitrogen-induced interface defects in Si oxynitride," *Physical Review B*, vol. 77, no. 10, article 104108, 2008.

[90] L. H. Ko, B. J. Cho, Y. B. Nga, and L. H. Chan, "The effect of nitrogen incorporation into the gate oxide by using shallow implantation of nitrogen and drive-in process," in *Proceedings 1998 Hong Kong Electron Devices Meeting (Cat. No.98TH8368)*, pp. 32–35, Hong Kong, China, 1998.

[91] D. E. Yildiz, D. H. Apaydin, E. Kaya, S. Altindal, and A. Cirpan, "The main electrical and interfacial properties of benzotriazole and fluorene based organic devices," *Journal of Macromolecular Science, Part A*, vol. 50, pp. 168–174, 2013.

[92] F. Tao, H. Yang, B. Tang et al., "TDDB characteristic and breakdown mechanism of ultra-thin SiO_2/HfO_2 bilayer gate dielectrics," *Journal of Semiconductors*, vol. 35, no. 6, pp. 064003–064009, 2014.